SCIENCE CHINA
Information Sciences

• RESEARCH PAPER •

December 2023, Vol. 66 222301:1–222301:15
https://doi.org/10.1007/s11432-022-3734-0

Prediction of fiber Rayleigh scattering responses based on deep learning

Yongxin LIANG[1], Jianhui SUN[1], Jialei ZHANG[1], Yuyao WANG[1], Anchi WAN[1], Shibo ZHANG[1], Zhenyu YE[1], Shengtao LIN[1] & Zinan WANG[1,2*]

[1]*Key Lab of Optical Fiber Sensing and Communications, University of Electronic Science and Technology of China, Chengdu* 611731*, China;*
[2]*Center for Information Geoscience, University of Electronic Science and Technology of China, Chengdu* 611731*, China*

Received 1 December 2022/Revised 20 February 2023/Accepted 6 April 2023/Published online 24 October 2023

Abstract Distributed acoustic sensing (DAS) is a fiber sensing technology based on Rayleigh scattering, which transforms optical fiber into a series of sensing units. It has become an indispensable part in the field of seismic monitoring, vehicle tracking, and pipeline monitoring. Fiber Rayleigh scattering responses lay at the core of DAS. However, there are few in-depth studies on the purpose of acquiring fiber Rayleigh scattering responses. In this paper, we establish a deep learning framework based on the bidirectional gated recurrent unit, which is the first time to predict the fiber Rayleigh scattering responses, to the best of our knowledge. The deep learning framework is trained with a numerical simulation dataset only, but it can process experimental data successfully. Moreover, since the responses could have a wider effective bandwidth than the experimental probing pulses, a finer spatial resolution could be obtained after demodulation. This work indicates that the deep learning framework can capture the characteristics of the fiber Rayleigh scattering responses effectively, which paves the way for intelligent DAS.

Keywords distributed acoustic sensing, Rayleigh scattering, deep learning, bidirectional gated recurrent unit, intelligent demodulation

Citation Liang Y X, Sun J H, Zhang J L, et al. Prediction of fiber Rayleigh scattering responses based on deep learning. Sci China Inf Sci, 2023, 66(12): 222301, https://doi.org/10.1007/s11432-022-3734-0

1 Introduction

Distributed acoustic sensing (DAS) has made significant progress in recent years. It can turn an optical fiber into a series of sensing units with the advantages of high sensitivity and fast response. It has thereby received extensive attention in the areas of seismic monitoring [1], vehicle tracking [2, 3], and pipeline monitoring [4].

The understanding of fiber Rayleigh scattering responses is particularly important, which is fundamental to the DAS study. Such responses originate from Rayleigh scattering in fiber, which is induced by localized inhomogeneities of the refractive index [5]. The characteristics of the fiber Rayleigh scattering responses will be affected by the external perturbation, because the external perturbation changes the refractive index and the length of fiber [6].

In conventional DAS schemes, the available sensing signal is the convolution of the fiber Rayleigh scattering responses and the probe pulse [7], whereas the fiber Rayleigh scattering responses are unknown. There are two reasons that few references delved into acquiring the fiber Rayleigh scattering responses: the first reason is that, in many applications, the external perturbation can be demodulated with the available sensing signal, without the knowledge of fiber Rayleigh scattering responses [8, 9]. The second reason is that it is intuitively difficult to capture the characteristics of the fiber Rayleigh scattering responses, because of their complex randomness over the fiber length [10, 11]. Despite the above reasons, if the fiber Rayleigh scattering responses can be predicted, it will bring about more possibilities. With

* Corresponding author (email: znwang@uestc.edu.cn)

such information, researchers can forecast sensing signals by numerical calculations without experimental testing, so that the sensing system could be optimized efficiently, opening a new window for intelligent DAS or other research, such as random fiber laser. Therefore, we investigate the implementation of deep learning technology in DAS, for the purpose of predicting fiber Rayleigh scattering responses.

Nowadays, many artificial intelligence (AI) algorithms have been applied in DAS signal processing to realize pattern recognition [3,12–14], noise suppression [15–18], and high computational efficiency [19,20]. Pattern recognition is to identify the type of perturbation signals. In [13], a generative adversarial network (GAN) is used to produce DAS data as the training dataset, and as such the trained convolution neural network (CNN) will be more effective in distinguishing between noise, footsteps, and vehicles. Besides, DAS technology can make use of the existing underground communication optical fiber to classify the roughness level of the road with the support vector machine (SVM) [14]. In railway safety, with DAS technology demodulated by a convolutional long short-term memory neural network (ConvLSTM), the intrusion detection task can be realized by setting the optical fiber along the high-speed railway [3]. For noise reduction, the denoising convolutional neural network (DnCNN) was proposed in the field of computer vision for intelligent noise filtering, and it was successfully applied for filtering the Rayleigh scattering pattern in DAS system [18]. Similarly, an attention-based CNN was proposed for noise filtering, which can achieve a better denoising effect when DAS signals are collected in a short time [15]. Besides, a one-dimensional CNN accepts the demodulated perturbation signal and the magnitude of the sensing signal as input, realizing various noise filtering including the laser frequency drift, laser phase noise, and interference fading [16]. In addition, SVM can be used to reduce the compensation residual error of the phase noise by using the compensation fiber with the scatter-enhanced points array [17, 21]. In terms of the DAS system based on cross-correlation demodulation, the demodulation procedure is quite time-consuming, especially in the case of long-distance sensing and fine spatial resolution. With the help of ANN, the demodulation speed can be improved [19, 20].

However, there are few studies about using AI for DAS system modeling and design. Previously, our group modeled the DAS system using CNN, and performed preliminary numerical simulations and experimental verifications, proving that the sensing system could be optimized efficiently [22, 23]. However, the weights and biases of CNN had to be constantly re-adjusted due to the robustness issue, resulting in a lack of practicability. It should be noted that, in other fields, there are examples of system modeling with AI. In optical communication, it can get smaller bit error rates through end-to-end modeling of the system by ANN [24]. In computational imaging, PhysenNet combines the physical model with the CNN to calculate original phase imaging without large dataset training [25]. In the weather forecast, radar observations from 20 min ago will be available to generate the predicted precipitation fields for the next 90 min, attributed to the successful modeling of the GAN network from the historical dataset [26]. The research objects in these examples are significantly different from DAS, so these methods cannot be used for DAS modeling.

In this paper, after comprehensive research, we establish a deep learning framework based on the bidirectional gated recurrent unit (BiGRU) to predict fiber Rayleigh scattering responses. The deep learning framework is trained through numerical simulation datasets only, and its effectiveness is verified with experimental data, which means that the proposed deep learning framework successfully captures the general characteristics of fiber Rayleigh scattering responses. In detail, as the proof-of-concept experiment, a heterodyne detection phase-sensitive optical time-domain reflectometry (Φ-OTDR) was implemented. The sensing signal was activated by two pulses with the same pulse duration, but with a time delay and a frequency shift; the trained deep learning framework receives the sensing signal and generates the fiber Rayleigh scattering responses, with a wider effective bandwidth than the probing pulse; then phase- and cross-correlation demodulation algorithms are respectively applied on the generated responses, the perturbation can be successfully demodulated, and with a finer spatial resolution than that determined by the pulse width.

2 Principle

2.1 Heterodyne detection Φ-OTDR

Rayleigh scattering, caused by localized inhomogeneities of the refractive index during fiber manufacture, is the feedback mechanism for DAS [5]. The fiber Rayleigh scattering responses can be treated as a set of

N scatterers at different positions and reflectivity [10], which can be approximated defined as (without taking polarizations into account) [11] :

$$\sum_{k=1}^{N} \bar{a}_k \delta\left(t-\tau_k\right), \tag{1}$$

where $\bar{a}_k = a_k \exp(-\alpha_0 v_g \tau_k)$. The τ_k and a_k represent the time delay and reflectivity, respectively, of the k-th scatterer. The α_0 is the attenuation coefficient of fiber. The v_g is the velocity of light in the fiber core. The N is the number of scatterers, and $\delta\left(t-\tau_k\right)$ is delta function where $\delta\left(0\right)=1$ and zero otherwise.

Eq. (1) implies that the scatterers are randomly located in the fiber. Another simplification is that the scattering elements are equally spaced in the fiber, but each scattering element has a different phase shift factor ϕ_k, which can be defined as

$$h_p(t) = \sum_{k=1}^{N} \bar{a}_k \exp(-\mathrm{j}\phi_k)\delta\left(t-k\Delta t\right), \tag{2}$$

where Δt is the time interval between the scatterers. The recovering of the scattering elements is intuitively difficult, because the relative time interval of two adjacent scatterers is too short to be distinguished by current analog-to-digital converters. Fortunately, with heterodyne detection, we can obtain the fiber Rayleigh scattering responses $h(t)$, generated by the scattering elements $h_p(t)$ through down-conversion, and can be written as

$$h(t) = G \cdot h_p(t) \cdot \exp(-\mathrm{j}\omega t), \tag{3}$$

where ω is the angular frequency of the local oscillator (LO) light, G is the gain introduced by the photoelectric detector and LO light. We substitute (3) into (2) and get

$$h(t) = G \cdot \sum_{k=1}^{N} \bar{a}_k \exp(-\mathrm{j}\Phi_k)\delta\left(t-k\Delta t\right), \tag{4}$$

where $\Phi_k = k\omega\Delta t + \phi_k$ is the synthesized delayed phase of the k-th scatterer. Finally, the received sensing signal $y(t)$ can be expressed simply in this form:

$$y(t) = m(t) * h(t) + n(t), \tag{5}$$

where $m(t)$ is the modulated pulse generated by arbitrary waveform generator (AWG) in the experiment, $n(t)$ is considered as additive white Gaussian noise (AWGN). The operation symbol $*$ is the convolution.

2.2 The principle of the GRU

The GRU network, which was proposed in 2014 [27], is a kind of recurrent neural network (RNN). It has less computation than a long short-term memory (LSTM) network. The common feature of these neural networks is that their output is not only related to the current input but also related to the previous input. The architecture of the GRU network is shown in Figure 1 and it contains four equations.

The reset gate r_n and the update gate z_n are computed as follows:

$$r_n = \sigma_g\left(W_r x_n + b_r + R_r s_{n-1}\right), \tag{6}$$

$$z_n = \sigma_g\left(W_z x_n + b_z + R_z s_{n-1}\right), \tag{7}$$

where σ_g is the sigmoid activation that forces their values to lie in the interval from 0 to 1. When the value is one or zero, the gate will be fully opened or closed. The x_n is the input vector at the n-th time step. The s_{n-1} is the previous hidden state.

The candidate state $\tilde{s}_n$ and the hidden state s_n are computed as follows:

$$\tilde{s}_n = \sigma_s\left(W_{\tilde{s}} x_n + b_{\tilde{s}} + r_n \odot \left(R_{\tilde{s}} s_{n-1}\right)\right), \tag{8}$$

$$s_n = \left(1-z_n\right) \odot \tilde{s}_n + z_n \odot s_{n-1}, \tag{9}$$

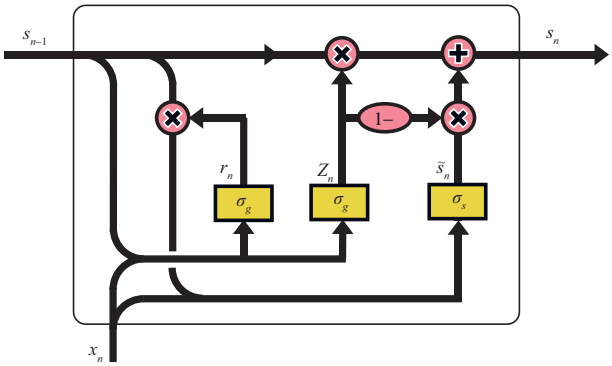

Figure 1 (Color online) The architecture of the GRU network.

where σ_s is the tanh activation function. The input weights $W_{r,z,\tilde{s}}$, the recurrent weights $R_{r,z,\tilde{s}}$ and the biases $b_{r,z,\tilde{s}}$ are the learnable variables. The operation symbol $\odot$ is the dot product.

From (8), we can see that the reset gate r_n determines how much information from the previous hidden state s_{n-1} will be retained in the current candidate state $\tilde{s}_n$. In (9), the calculation of hidden state s_n is the final pace of each time step. The update gate z_n determines whether the output hidden state s_n is closer to the current candidate state $\tilde{s}_n$ or the previous hidden state s_{n-1}.

In the task of predicting fiber Rayleigh scattering responses, the use of the GRU network has advantages. On the one hand, the GRU network usually has fewer training parameters, which will force the GRU network to find the optimal parameters to fit the relatively large training dataset. As a result, higher performance will be achieved on the test dataset. On the other hand, the GRU network is adept at extracting time-series features and is particularly suited to predicting the time-series characteristics of fiber Rayleigh scattering responses. This is achieved through the cooperation of the reset and update gates, allowing the GRU network to remove or add previous information.

2.3 The proposed deep learning framework

In this subsection, we describe the details of the proposed scheme based on the above principles. Its architecture is shown in Figure 2, which describes the relationship between the input space, the BiGRU network, and the output space.

Since neural networks cannot deal with the complex signal, the complex signal will be split into the real and imaginary components. Thus, the input $\boldsymbol{I}_n$ is the concatenation of the envelope, real component, and imaginary component of the sensing signal at the n-th sampling point along the distance axis. Besides, the input $\boldsymbol{I}_n$ has a parameter α that can adjust the output performance of the BiGRU network. The output $\boldsymbol{O}_n$ is the concatenation of the real and imaginary components of the fiber Rayleigh scattering responses at the n-th sampling point along the distance axis.

During the training stage, the parameter α is determined based on the signal-to-noise ratios (SNRs) of the sensing signals, which will be described in Subsection 2.5. Additionally, further elaboration and discussion of the parameter α are provided in Subsection 2.6.1.

The deep learning framework is trained using a numerical simulation dataset that contains the general characteristics of fiber Rayleigh scattering responses. Through training, the neural network can capture these characteristics. Given a particular fiber under test to be studied in the experiment, we must first obtain the sensing signal as the input to the trained neural network. The neural network will then generate the fiber Rayleigh scattering responses for the particular fiber under test.

2.4 Generating datasets for the deep learning framework with preprocessing program

Here, we generate the sensing signal and the fiber Rayleigh scattering responses according to parameters shown in Table 1 through numerical simulation. Then, to reduce the data redundancy, these data undergo a preprocessing program to form training, validation, and test datasets.

2.4.1 *Generating signals through numerical simulation*

The following is a description of the training dataset, while the description of the validation and test datasets are the same, only the parameters are different. To build the training dataset, the fiber Rayleigh

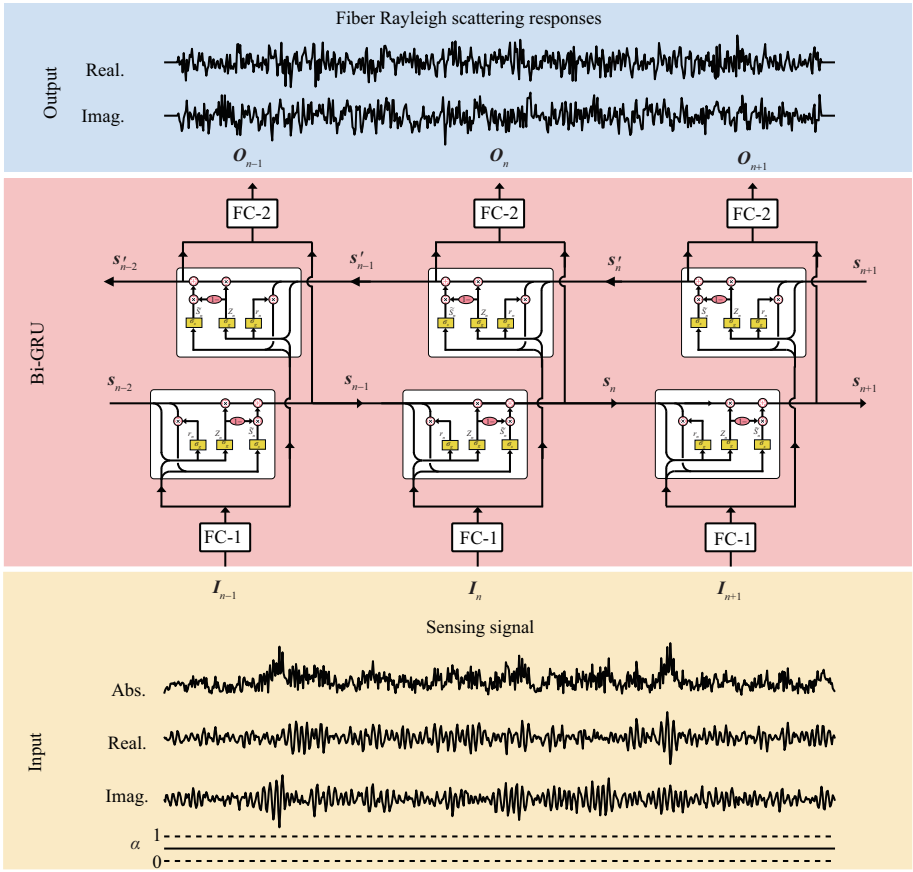

Figure 2 (Color online) The architecture of the proposed deep learning framework.

Table 1 Parameters of the training and test dataset

Parameters	Training dataset	Validation dataset	Test dataset
Fiber length (m)	500	500	10000
Number of fiber	475	25	1
Number of copies	20	20	1
Sampling rate (GHz)	1	1	1
SNR of sensing signals (dB)	0–10 (Step: 2 dB)	0–10 (Step: 2 dB)	−4–12 (Step: 1 dB)

scattering responses with the number of 475 and the length of 500 m will be generated at 1 GHz sampling rate, which means the time step Δt is 1 ns in (4). Assume that the fiber Rayleigh scattering responses are zero-mean circularly symmetric complex Gaussian random variables. In this way, the envelope of the responses will obey the Rayleigh distribution, the phase will obey the uniform distribution, and the real and imaginary components will obey the Gaussian distribution.

As for the modulation pulse, it consists of two pulses with the same duration of 100 ns, with an interval of 20 ns between the two pulses and different center frequencies of 310 and 265 MHz, respectively. Then, the sensing signal is generated according to (5), which will be added to AWGN. Due to the random nature of noise, 20 copies of each sensing signal are created before the noise is added, which will help the deep learning framework to learn noise reduction. The sensing signals will be adjusted to have different power levels for the signal and noise components, resulting in a range of SNRs from 0 to 10 dB at a step of 2 dB.

2.4.2 *The preprocessing program*

The sensing signals need to be preprocessed before generating the training and test dataset. Firstly, the preprocessing program extracts the sensing signals in the frequency range of 235 to 350 MHz by bandpass filtering. Then, the filtering signals will be digitally down-converted to baseband signals centered at a

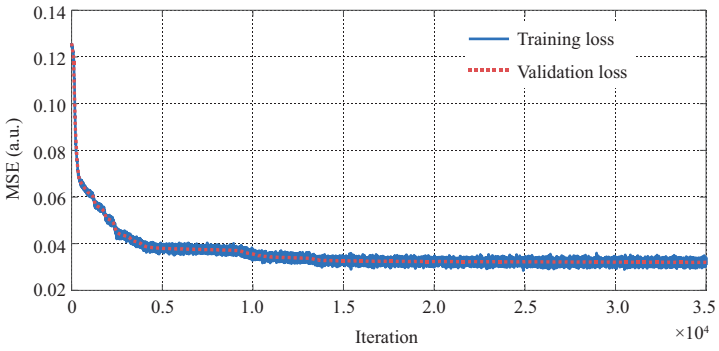

Figure 3 (Color online) Training MSE for each iteration.

zero frequency, with a down-conversion frequency of 287.5 MHz. After that, the sensing signals can be down-sampled at 125 MHz without aliasing in the frequency domain, which completes the construction of the input space for the training dataset. Similarly, the fiber Rayleigh scattering responses as the output space are preprocessed in the same way. After preprocessing, redundant data can be removed and the deep learning framework can perform feature extraction more easily.

2.5 Training the deep learning framework

The deep learning framework consists of FC-1, BiGRU, and FC-2, as shown in Figure 2. FC-1 contains a fully connected layer with 20 nodes and a Relu layer for initial feature extraction. FC-2 has a fully connected layer with 2 nodes for synthesizing the results of the hidden states in BiGRU and outputting the real and imaginary components of fiber Rayleigh scattered responses. The BiGRU consists of two GRUs in opposite directions, which allows the neural network to synthesize the information passed forward and backward at each time step. The adaptive moment estimation (Adam) optimizer is selected for training with a learning rate of 0.0003 and a mini-batch of 200. The mean squared error (MSE) is used as the loss function during training. It takes nearly 4 h to complete 35000 iterations. Figure 3 displays the curves of training and validation loss, which indicate good convergence.

During the training stage, the value of parameter α varies between 0 and 1 based on the SNR of the samples. It takes on specific values of $\{0, 0.2, 0.4, 0.6, 0.8, 1\}$ corresponding to the discrete SNR values of $\{0, 2, 4, 6, 8, 10\}$ dB. The value of parameter α indicates the level of SNR in each training sample. By using parameter α to differentiate between samples, the neural network is able to produce different output characteristics. This is achieved by applying different noise suppression strategies to training samples with different SNRs, for the purpose of minimizing training loss during the training stage.

2.6 Examining the effectiveness of the deep learning framework

After the training stage, two test samples are selected from the test dataset for observation in the frequency domain, as presented in Figures 4(b) and (c). These two samples have different SNRs but share the same ground truth.

Before moving on, defining the SNR is crucial to prevent any potential confusion. Before preprocessing, test sample I has 10 dB SNR, and test sample II has 0 dB SNR. After preprocessing, the SNRs of these two samples are increased to 19.7 and 9.7 dB, respectively, due to bandpass filtering in the preprocessing program. However, for convenience, the SNRs reported in this paper refer to the results before preprocessing, rather than after preprocessing. Besides, the SNR defined here is the ratio of the signal power to the noise power, rather than the ratio of the highest peak power to the noise level in the frequency domain.

After preprocessing, the ground truths of the test dataset in the frequency domain are shown in Figures 4(a) and (d). The frequency range from -62.5 to 62.5 MHz, since the sampling rate is 125 MHz. Figure 4(a) displays the ground truths of the input sensing signal, revealing that the signal contains not only two primary lobes but also first and second side lobes. Correspondingly, Figure 4(d) shows the ground truths of the output. Since the fiber Rayleigh scattering responses are assumed to be zero-mean circularly symmetric complex Gaussian random variables, they have a flat envelope in the frequency domain, as shown by the red solid line in Figure 4(d).

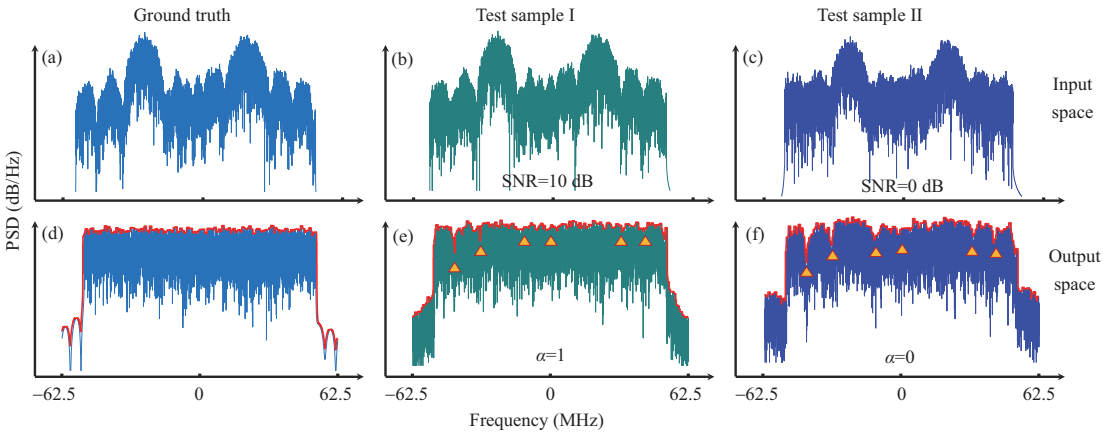

Figure 4 (Color online) The ground truths of the test dataset in the frequency domain: (a) the input space; (d) the output space. The frequency domain of the input signal in (b) SNR = 10 dB and (c) SNR = 0 dB. The corresponding outputs of the deep learning framework in the frequency domain, under (e) $\alpha = 1$ and (f) $\alpha = 0$.

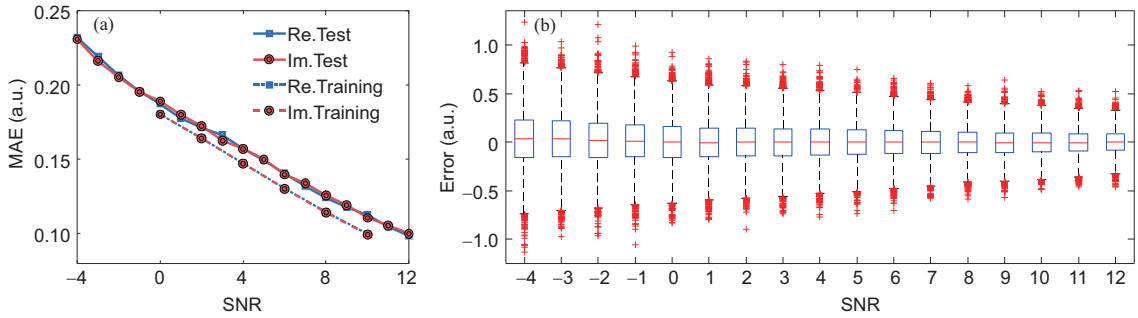

Figure 5 (Color online) (a) The MAE versus SNR. The real and imaginary components of the test datasets are represented as Re.Test and Im.Test, respectively, while the real and imaginary components of the training datasets are represented as Re.Training and Im.Training, respectively. (b) The summary statistics of predicted errors at different SNRs for the test datasets.

2.6.1 *Investigating the role of parameter α*

As can be seen from Figures 4(b) and (c), the side lobes are easily drowned out by the noise. In this case, the parameter α is designed to help the deep learning framework to reconstruct the fiber Rayleigh scattering responses. Setting α between one and zero can change the output characteristics. For example, the α is set to one in test sample I, and is set to zero in test sample II. As can be seen in Figures 4(e) and (f), the flatness of the output envelope in the frequency domain is inconsistent, especially at the markings of the yellow triangles. The deep learning framework will suppress the power at the markings when the α is zero. Due to the characteristics of the input signal, these markings are easily swamped by noise. The output will leave valid information and suppress those that are drowned out by noise. This suppression can be adjusted by the value of α.

It should be noted that without the parameter α, the neural network would not be able to get this capability as mentioned above. The parameter α guides the network training. It informs the neural network which training samples have a high SNR ($\alpha = 1$) and which have a low SNR ($\alpha = 0$). This allows the neural network can distinguish between samples, and generate different characteristics of the output. This is because the neural network can perform different noise suppression strategies for sensing signals with different SNRs, in order to minimize the training loss during the training stage. Without the parameter α, the neural network cannot perform the different strategies, and it will try to recover the ground truths for all training samples as far as possible, without the ability to eliminate the noise at the locations marked by yellow triangles in Figure 4.

2.6.2 *Evaluating the error and its significance*

Mean absolute error (MAE) was calculated separately for the real and imaginary components of the complex vector (i.e., the predicted fiber Rayleigh scattering responses), as shown in Figure 5(a).

The calculations were performed under different SNR samples, using the following formulas for the

real and imaginary components:

$$\mathrm{MAE_{Re}} = \frac{1}{N}\sum_{i=1}^{N}\left|\mathrm{Re}\left(h_i\right) - \mathrm{Re}(\bar{h_i})\right|, \tag{10}$$

$$\mathrm{MAE_{Im}} = \frac{1}{N}\sum_{i=1}^{N}\left|\mathrm{Im}\left(h_i\right) - \mathrm{Im}(\bar{h_i})\right|, \tag{11}$$

where $\mathrm{Re}(h_i)$ and $\mathrm{Im}(h_i)$ represent the real and imaginary components of the actual value, and $\mathrm{Re}(\bar{h_i})$ and $\mathrm{Im}(\bar{h_i})$ represent the real and imaginary components of the predicted value, respectively. The N represents the number of points along the distance axis. As depicted in Figure 5(a), the marginal difference between the test dataset error and the training dataset error suggests that the neural network exhibits strong generalization capabilities. The real and imaginary components display similar error levels, suggesting that the deep learning framework generates output without bias. The error increases smoothly as the SNR decreases, without any sharp increases. These results imply that the deep learning framework is robust to different SNRs in the test dataset.

Figure 5(b) shows the box plot, which summarizes the statistics of predicted errors for the test samples with different SNRs. For illustration purposes, the blue box with 0 dB SNR is used as an example. The median of the predicted errors, indicated by the central red line, is -0.001. The edges of the blue box represent the 25th and 75th percentiles of the error distribution, which are -0.16 and 0.16, respectively. The whiskers, represented by dashed black lines, extend to the most extreme error points that are not considered as outliers, which are -0.83 and 0.93, respectively. Outliers are individually plotted using red '+' markers, and there are 75 outliers, which represent 0.62% of the total points (N) of the test sample with 0 dB SNR.

3 Results and discussion

A heterodyne detection Φ-OTDR was built to acquire the sensing signals as described in Subsection 3.1. The signal processing flow chart is discussed in Subsection 3.2. The acquired sensing signals were then processed by the deep learning framework to predict the fiber Rayleigh scattering responses, as described in Subsection 3.3. The discussion and analysis of the proposed method are presented in Subsection 3.4.

3.1 Experiment setup

The experimental setup is shown in Figure 6(a). A 1550 nm ultra-narrow linewidth laser (NKT, E15) provides a continuous wave (CW) light source for the transmitter and receiver, respectively, via the optical coupler 1 (OC-1). The 99% port of OC-1 is connected to the acoustic optical modulator (Gooch & Housego, T-M300-0.1C16J-3-F2P) to generate the probe pulse, which consists of two pulses of the same duration of 100 ns, with an interval of 20 ns between the two pulses and different frequency shifts of 310 and 265 MHz, respectively. The probe pulse is then launched into the 11.2 km sensing fiber through the circulator (CIR) with a repetition period of 120 μs, and the Rayleigh backscattering (RBS) lightwave is returned from the same circulator to the receiver. The CW light from the 1% port of OC-1 is served as the LO light. The receiver will mix the RBS lightwave with the LO light at the 3 dB optical coupler (OC-2). The polarization state of LO light can be modified by the polarization controller (PC) to reduce polarization mismatch loss. The variable optical attenuator (VOA) is used to adjust the power of LO light to a suitable value. Then, the sensing signal will be detected by a balanced photodetector (Thorlabs, PDB470C) with 400 MHz bandwidth and sampled at 1 GHz by the oscilloscope (OSC).

To demonstrate the dynamic strain sensing capacity, the piezoelectric ceramic transducer (PZT) is loaded with a sinusoidal signal with a frequency of 400 Hz and a voltage peak-to-peak of 2.5 V, as the external perturbation. Two 1.5-meter fibers are wrapped around the PZT. Between these two fibers, there is an 8.4 m fiber that is not wrapped by the PZT. Such a wrapping scheme can demonstrate the improved spatial resolution of the proposed method.

3.2 An overview of signal processing

The signal flow diagrams are shown in Figure 6(b). For the traditional method, the sensing signals obtained at intermediate frequency are subjected to Hilbert transform to obtain complex vectors. Subse-

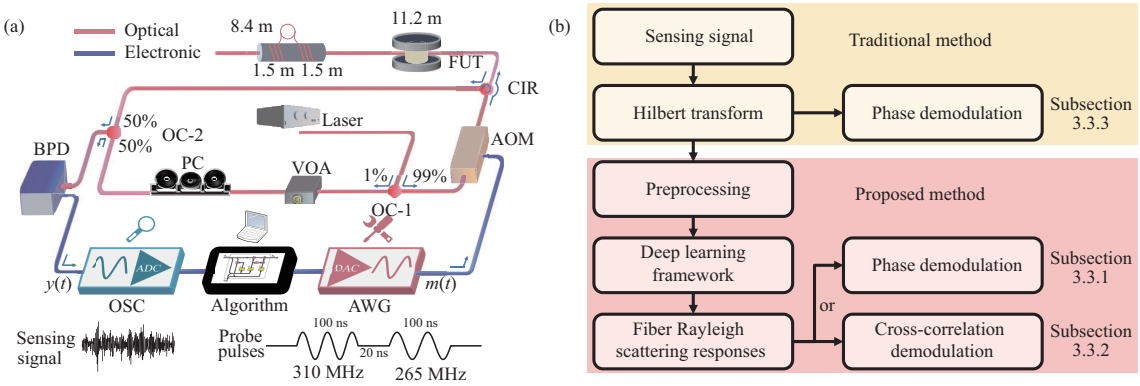

Figure 6 (Color online) (a) Experimental setup of 11.2 km Φ-OTDR. AOM: acoustic optical modulator; BPD: balanced photodetector. (b) The signal flow diagrams.

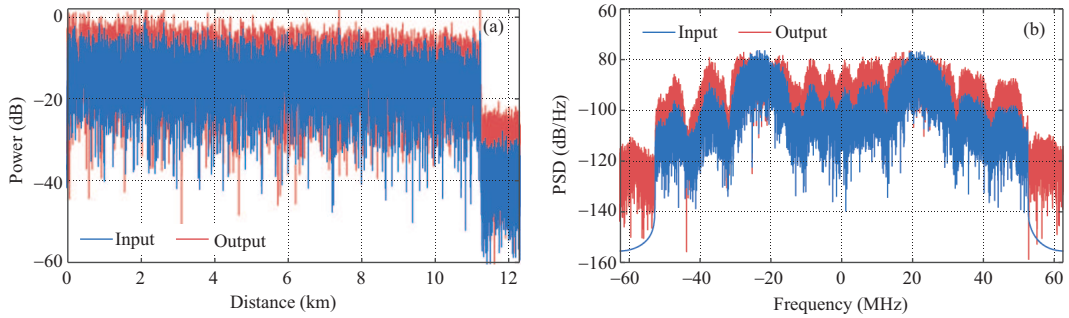

Figure 7 (Color online) Comparision of the input and output in (a) the distance domain and (b) the frequency domain.

quently, phase demodulation is applied, which involves fading suppression, and phase unwrapping, phase differential approaches, and the results are reported in Subsection 3.3.3.

In contrast, for the proposed method, the complex vector resulting from the Hilbert transform is first processed by the preprocessing program, as previously described in Subsection 2.4.2. Next, the preprocessed signals will be fed into the deep learning framework, which were first analyzed in a numerical simulation described in Subsection 2.6, and will be further evaluated in the experiment presented in Subsection 3.3. Two demodulation methods based on fiber Rayleigh scattering responses are presented: phase demodulation in Subsection 3.3.1 and cross-correlation demodulation in Subsection 3.3.2. The results of these demodulation techniques will be compared with those of the traditional method in Subsection 3.3.3.

3.3 Prediction of the fiber Rayleigh scattering responses

In this subsection, the fiber Rayleigh scattering responses are predicted by the proposed framework. Subsequently, either phase or cross-correlation demodulation methods can be used. This is because arbitrary sensing signals can be calculated from the fiber Rayleigh scattering responses, satisfying the conditions of the phase or cross-correlation demodulation algorithm. In this way, the external perturbations can be distinguished by reconfiguring the spatial resolution. In general, phase demodulation is computationally faster than cross-correlation demodulation, while the results of cross-correlation demodulation are not affected by fading.

The input is the sensing signal after Hilbert transform and preprocessing. The output is the fiber Rayleigh scattering responses. The parameter α is set to 0. The power of the sensing signal is shown in Figure 7(a). The output power is slightly higher than the input, and the reason can be found in the frequency domain. As depicted in Figure 7(b), certain frequency components in the sidelobes of the output signal demonstrate increased power compared to the input signal. However, the power of the null points between the side lobes will not be amplified.

Table 2 Parameters of sub-chirped pulses in different demodulation methods

Parameters	Phase demodulation	Cross-correlation demodulation
Center frequency (f_c) (MHz)	−35–35 (Step: 5 MHz)	−42–42 (Step: 1 MHz)
Duration (D) (μs)	2	50
Sweeping bandwidth (B) (MHz)	25	20
Total number	15	84

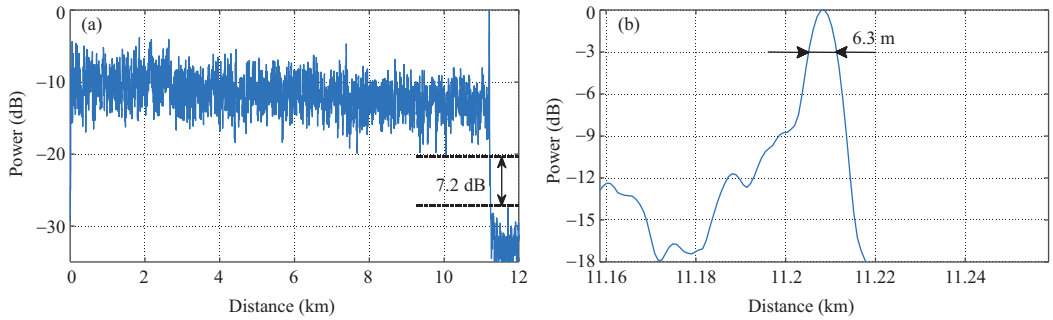

Figure 8 (Color online) (a) Normalized power trace processed after fading elimination; (b) reflection point at the end of the sensing fiber.

3.3.1 *Phase demodulation based on the fiber Rayleigh scattering responses*

In this subsection, we briefly review the development of phase demodulation and fading elimination methods for the sensing signal. Then, a suitable demodulation scheme is selected, to demonstrate the advantage of demodulation based on the fiber Rayleigh scattering responses.

In phase demodulation, the differential phase, which contains the information of external perturbation, can be obtained by setting time-delay interference of the RBS signal [28]. It can also be obtained by homodyne detection [8] or heterodyne detection [9], after applying the phase unwrapping algorithm and phase differential on the sensing signal. Although the effect of phase demodulation will be affected by fading issues, there are various approaches for fading elimination, such as the rotated-vector-sum (RVS) method [29], spectrum extraction and remix method [30] for interference fading elimination, or polarization multiplexing and diversity for polarization fading elimination [31].

These are the phase demodulation and fading elimination methods for the sensing signal. Once the fiber Rayleigh scattering responses are obtained, we could calculate the sensing signals of multiple sub-chirped pulses with matched filters, which can be expressed as

$$y'_m(t) = h'(t) * c_m(t) * c^*_m(-t), \tag{12}$$

where $h'(t)$ are the predicted fiber Rayleigh scattering responses generated by the deep learning framework, $c_m(t) = \exp\left(\mathrm{j} \cdot 2\pi(f_m t + kt^2/2)\right)$ is the m-th sub-chirped pulse, $c^*_m(-t)$ is the matched filter of the m-th sub-chirped pulse, $f_m = f_c - B/2$ is the stat frequency, f_c is the center frequency, B is the sweeping bandwidth, $k = B/D$ is the chirp rate, and D is the duration of the sub-chirped pulse. The detailed parameters of the chirped pulses are shown in Table 2. The center frequency ranges from −35 to 35 MHz at a step of 5 MHz. It should be noted that, the sweeping frequency range of the sub-chirped pulse $c_m(t)$ cannot exceed the effective bandwidth of the recovered fiber Rayleigh scattering responses.

The RVS method is used to remix the predicted sensing signals of the 15 sub-chirped pulses for fading elimination [30]. One of the normalized power traces processed by the RVS method is shown in Figure 8(a). the lowest power point is 7.2 dB higher than the noise area, which means it is free of fading. The full width at half maximum of the reflection point is 6.3 m, as shown in Figure 8(b), indicating that the spatial resolution is 6.3 m.

The differential phase is generated by the phase unwrapping algorithm and phase differential [9] on the results of the RVS method. Given a parameter of 7.4 m gauge length, the differential phase versus time and distance is displayed in Figure 9(a), which reveals the presence of two perturbation signals at around 11.1 km. By calculating the standard deviation (SD) of the phase along the fiber, we can evaluate the fading suppression effect. If there are fading points, anomalous peaks will arise, which are caused by demodulation errors of the differential phase due to the fading point. But there are only two peaks in

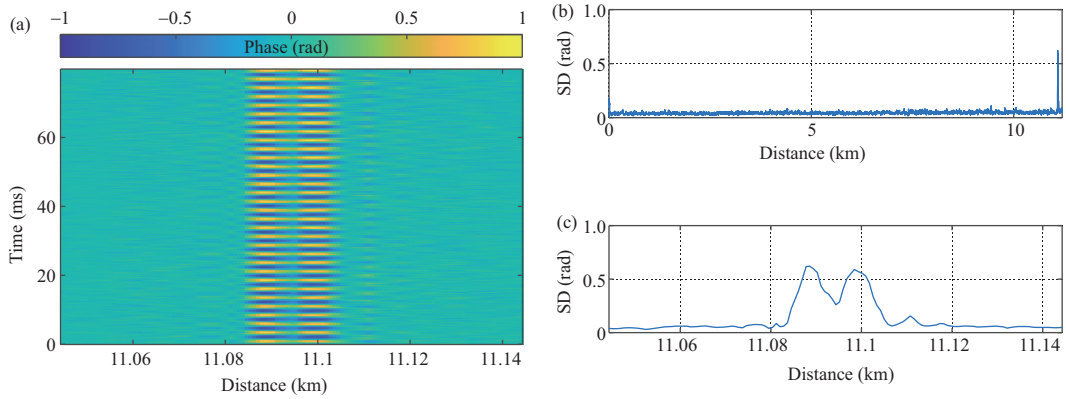

Figure 9 (Color online) Phase demodulation by the proposed method. (a) The differential phase in 7.4 m gauge length; (b) and (c) are the SD of differential phase in different observation ranges.

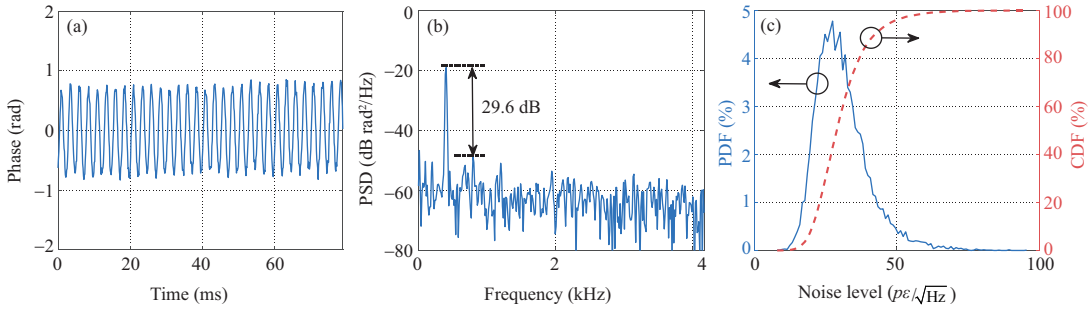

Figure 10 (Color online) Phase demodulation by the proposed method can distinguish between the two perturbations. (a) The time domain and (b) the frequency domain of the demodulated perturbation; (c) the PDF and CDF of the maximum noise level along the sensing fiber.

Figure 9(b), which is caused by external perturbations, indicating that it is free of fading. After zooming in on this position, we can clearly distinguish these two perturbations, as shown in Figure 9(c).

The time and the frequency domains of one of the demodulated perturbations are shown in Figures 10(a) and (b), respectively. The power spectral density (PSD) is calculated with the Hanning window, demonstrating that the demodulated signal has an SNR of 29.6 dB in the range of 0.05 to 4.16 kHz.

The noise level will fluctuate along the sensing fiber, because the envelope of the signal fluctuates along the fiber, as shown in Figure 8(a). Thus, we calculate the maximum noise level in the range of 0.05 to 4.16 kHz for all sensing points in front of the perturbation area. By performing statistics on the probability density function (PDF) and the cumulative distribution function (CDF), the maximum noise level is 61.0 $p\varepsilon/\sqrt{\text{Hz}}$ at 99% CDF, as shown in Figure 10(c).

3.3.2 *Cross-correlation demodulation based on the fiber Rayleigh scattering responses*

In this subsection, we first review the development of cross-correlation demodulation methods, and then the demodulation results are given.

As for the cross-correlation demodulation, single-shot measurement schemes based on chirped pulse modulation have been favored in recent years. It has no fading issue, but the calculation is relatively time-consuming compared with the phase demodulation. The basis of cross-correlation demodulation is that external perturbation will cause the time or frequency shift of the sensing signal. The time-shift measurement was proposed in 2016 with direct detection [32], showing good temperature or strain measurement ability. Whereafter, the non-matched filter was proposed to break the trade-off between spatial resolution and the pulse duration in the scheme of time-shift measurement with coherent detection [33]. Besides, the Rayleigh scattering patterns, versus frequency and distance, were generated by the sub-chirped-pulse extraction algorithm (SPEA) with coherent detection, and frequency-shift measurement can be realized along the frequency axis [34].

Theoretically, after obtaining the fiber Rayleigh scattering responses, time-shift measurement can be

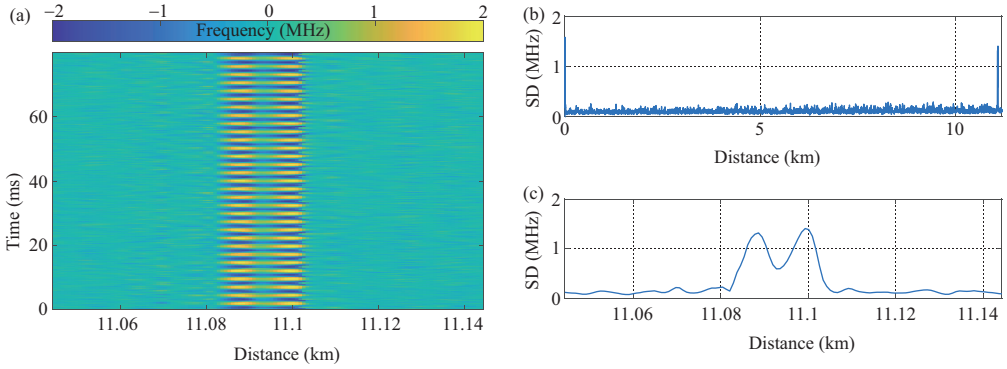

Figure 11 (Color online) Cross-correlation demodulation by the proposed method. (a) The demodulated frequency shift; (b) and (c) are the SD of the demodulated frequency shift for different observation ranges.

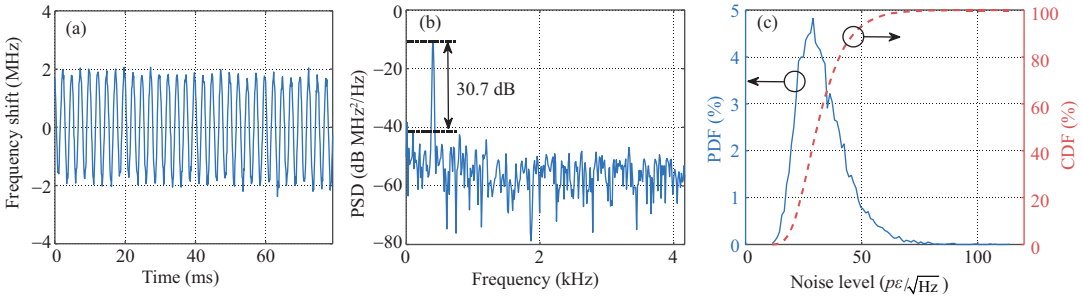

Figure 12 (Color online) Cross-correlation demodulation by the proposed method. (a) The time domain and (b) the frequency domain of the demodulated perturbation; (c) the PDF and CDF of the maximum noise level along the sensing fiber.

implemented based on the non-match filter method [33], and frequency-shift measurement can also be implemented based on the SPEA method [34]. Here, the latter method is used for demonstration. The predicted fiber Rayleigh scattering responses are demodulated by the SPEA method, and the parameters of the sub-chirped pulses are shown in Table 2.

The sweep bandwidth and the frequency step of each sub-chirped pulse are smaller than those in the phase demodulation. The range of center frequency is larger than that in the phase demodulation, from −42 to 42 MHz at a step of 1 MHz. Spline interpolation with a magnification of 50 is used to the cross-correlation results to better determine the frequency shifts. A Hanning window is used in a matched filtering approach to suppress the power of the sidelobe. Thus, the spatial resolution is attenuated to 7.4 m, which is the same as the gauge length in the phase demodulation.

Similar demodulation results can be obtained by cross-correlation demodulation. The demodulated frequency shift is shown in Figure 11(a). Two demodulated perturbations are located at around 11.1 km. The SD of the frequency shift is displayed in Figure 11(b), indicating that the demodulated frequency shift is free of fading. The two perturbations can also be clearly distinguished, as shown in Figure 11(c).

The time and the frequency domains of one of the demodulated perturbations are shown in Figures 12(a) and (b), respectively. The SNR of the demodulated perturbation is 30.7 dB in the frequency domain from 0.05 to 4.16 kHz. The PDF and the CDF for frequency are shown in Figure 12(c). The maximum noise level is 65.5 $p\varepsilon/\sqrt{\text{Hz}}$ at 99% CDF. To consider the relationship between the frequency shift and the phase, two equations are referred [30, 34]

$$\frac{\Delta v}{v_0} = K_\varepsilon \Delta\varepsilon, \tag{13}$$

$$\Delta\varepsilon = K_\phi \frac{\Delta\phi}{\text{GL}}. \tag{14}$$

Then we can get

$$\Delta\phi = \frac{\text{GL}}{K_\phi K_\varepsilon v_0} \Delta v, \tag{15}$$

where Δv and $\Delta\phi$ are the demodulated frequency shift and differential phase, respectively, $K_\varepsilon = -0.78$ and the K_ϕ is approximately 110 $n\varepsilon \cdot \text{m/rad}$, gauge length GL is 7.4 m. The frequency of the light v_0 is

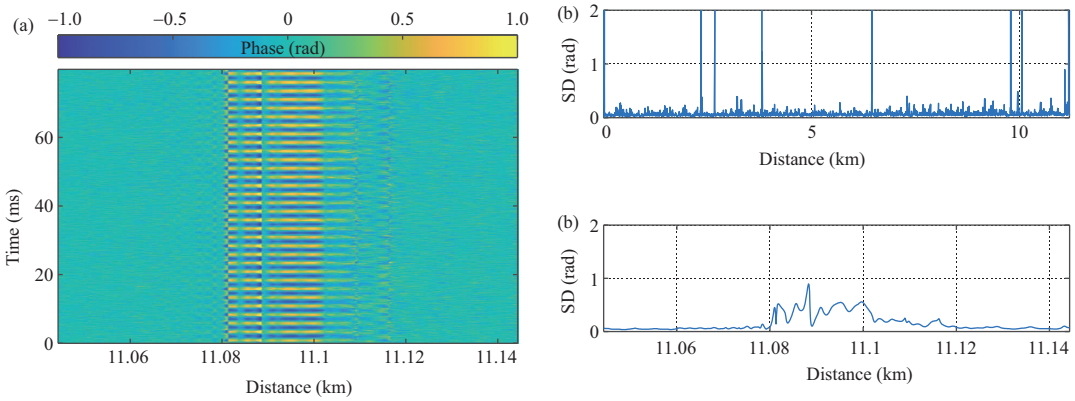

Figure 13 (Color online) Phase demodulation based on the sensing signal cannot distinguish between the two perturbations. (a) The differential phase in the perturbation zone with 7.4 m gauge length; (b) and (c) are the SD of differential phase.

approximately 193.5 THz. $\Delta\varepsilon$ is the applied strain. The amplitude of the demodulated frequency shift Δv is about 1.9 MHz. Its theoretical phase amplitude will be 0.83 rad according to (15) calculation, which is approximately the same compared to the phase amplitude of 0.74 rad in Figure 10(a).

3.3.3 *Phase demodulation based on the sensing signal*

In this subsection, phase demodulation based on the sensing signal is the traditional method, and the results are used to compare with the proposed method. It should be noted that without the proposed method, the sensing signals in this paper could not be demodulated by cross-correlation demodulation directly. Therefore, we only demonstrate the results of phase demodulation here.

We demodulate the sensing signal by the phase demodulation with the RVS method [29] for fading elimination. In detail, two bandpass finite impulse response filters are designed with passbands ranging from 300–320 MHz and 255–275 MHz. The two filters are separately convolved with the sensing signals, and these two convolution results need to be compensated for a time delay of 120 ns delay before applying the RVS method. After applying phase demodulation, the gauge length should be set larger than the 10 m spatial resolution. However, for comparison with the proposed method, the gauge length was set to 7.4 m.

The differential phase in the perturbation zone is shown in Figure 13(a), presenting an aliasing demodulation result. The SD of the differential phase calculated along the time axis is depicted in Figures 13(b) and (c). The presence of some peaks in Figure 13(b) indicates that the fading issue is not cleanly eliminated. Besides, it can be seen that these two external perturbations cannot be distinguished in Figure 13(c).

3.4 Discussion, limitation and advantage

In this subsection, an explanation is given for why the proposed method can achieve better demodulation than the traditional method. The limitations of this method are then analyzed for potential further improvement. Finally, the advantages of using a neural network are summarized.

For a more comprehensive understanding, an explanation is as follows. The fiber Rayleigh scattering responses are synthesized from the sensing signals, which were activated by two pulses with different carrier frequencies. The synthesized responses have a wider effective bandwidth than a single probing pulse, which leads to a finer spatial resolution when demodulating based on the responses. In contrast, the traditional method could not synthesize a wider effective bandwidth, which means that the spatial resolution is determined by the pulse width. Hence, compared to the traditional method, the proposed approach maximizes the use of sensing signal information.

While the proposed approach improves spatial resolution, it has a performance limitation. In order to further obtain an even finer spatial resolution, the fiber Rayleigh scattering responses with a wider bandwidth can be synthesized by launching multiple pulses with different carrier frequencies, which results in an increase in the size of the neural network to perform feature extraction over a wider frequency range, and hence increases the computational load.

Nevertheless, the use of neural networks has inherent advantages. First, the neural network is good at creating complicated and non-linear connections between inputs (sensing signals) and outputs (fiber Rayleigh scattering responses). This capability is well-suited for predicting fiber Rayleigh scattering responses due to their complex randomness over the fiber length. Second, the neural network has been trained on vast datasets, allowing it to make accurate predictions across a wide range of examples. As a result, the trained neural network is capable of adapting to signals with varying SNRs. Besides, since the presets in the numerical simulation are only related to the intermediate frequency, the trained neural network can work at other optical frequencies. That means the neural network will not require retraining when it is used in different lasers of different wavelengths.

4 Conclusion

In this paper, a deep learning framework is established to predict the fiber Rayleigh scattering responses for the first time. It was trained with the numerical simulation dataset only, but it can predict the wideband fiber Rayleigh scattering responses from experimental signals with dual-frequency features. By analyzing the results of both numerical simulation and experimental verification, it is assured that the deep learning framework successfully captures the general characteristics of the fiber Rayleigh scattering responses, bringing about more possibilities for DAS operations. Once these responses are obtained, either phase or cross-correlation demodulation can be used to demodulate the external perturbations flexibly, making it easier to fully utilize the wideband information for better demodulation than the conventional schemes.

Furthermore, with the deep learning framework, researchers can forecast sensing signals by numerical calculations without experimental testing, so that the sensing system could be optimized efficiently. The deep learning framework could also integrate various demodulation methods and combine their advantages, indicating that there is plenty of room for further research in intelligent signal processing in DAS research.

Acknowledgements This work was supported by National Natural Science Foundation of China (Grant No. 62075030), National Ten-Thousand Talent Program (Grant No. W030211001001), and Sichuan Provincial Project for Outstanding Young Scholars in Science and Technology (Grant No. 2020JDJQ0024).

References

1 Fernández-Ruiz M R, Soto M A, Williams E F, et al. Distributed acoustic sensing for seismic activity monitoring. APL Photonics, 2020, 5: 030901
2 Liu H Y, Ma J H, Xu T W, et al. Vehicle detection and classification using distributed fiber optic acoustic sensing. IEEE Trans Veh Technol, 2020, 69: 1363–1374
3 Li Z Q, Zhang J W, Wang M N, et al. Fiber distributed acoustic sensing using convolutional long short-term memory network: a field test on high-speed railway intrusion detection. Opt Express, 2020, 28: 2925
4 Li G, Zeng K H, Zhou B, et al. Vibration monitoring for the West-East Gas Pipeline Project of China by phase optical time domain reflectometry (phase-OTDR). Instrum Sci Tech, 2021, 49: 65–80
5 Bao X Y, Wang Y. Recent advancements in Rayleigh scattering-based distributed fiber sensors. Adv Dev Instrum, 2021, 2021: 8696571
6 Cranch G A, Nash P J. High-responsivity fiber-optic flexural disk accelerometers. J Lightwave Technol, 2000, 18: 1233–1243
7 Liang Y X, Wang Z N, Lin S T, et al. Optical-pulse-coding phase-sensitive OTDR with mismatched filtering. Sci China Inf Sci, 2022, 65: 192303
8 Wang Z N, Zhang L, Wang S, et al. Coherent Φ-OTDR based on I/Q demodulation and homodyne detection. Opt Express, 2016, 24: 853
9 Jiang J L, Wang Z N, Wang Z T, et al. Coherent Kramers-Kronig receiver for Φ-OTDR. J Lightwave Technol, 2019, 37: 4799–4807
10 Park J, Lee W, Taylor H F. Fiber optic intrusion sensor with the configuration of an optical time-domain reflectometer using coherent interference of Rayleigh backscattering. In: Proceedings of Photonics China'98, Beijing, 1998. 49–56
11 Healey P. Fading in heterodyne OTDR. Electron Lett, 1984, 20: 30
12 Zhang X Z, Sun H N, Jiang J F, et al. Optical time-series signals classification based on data augmentation for small sample. Sci China Inf Sci, 2022, 65: 229303
13 Shiloh L, Eyal A, Giryes R. Efficient processing of distributed acoustic sensing data using a deep learning approach. J Lightwave Technol, 2019, 37: 4755–4762
14 Huang M F, Ji P, Wang T, et al. First field trial of distributed fiber optical sensing and high-speed communication over an operational telecom network. J Lightwave Technol, 2020, 38: 75–81
15 Wang M N, Deng L, Zhong Y Z, et al. Rapid response DAS denoising method based on deep learning. J Lightwave Technol, 2021, 39: 2583–2593
16 Jiang F, Zhang Z H, Lu Z X, et al. High-fidelity acoustic signal enhancement for phase-OTDR using supervised learning. Opt Express, 2021, 29: 33467
17 Liu T, Li H, He T, et al. Ultra-high resolution strain sensor network assisted with an LS-SVM based hysteresis model. Opto-Electron Adv, 2021, 4: 200037

18 Liehr S, Borchardt C, Münzenberger S. Long-distance fiber optic vibration sensing using convolutional neural networks as real-time denoisers. Opt Express, 2020, 28: 39311
19 Liehr S, Jäger L A, Karapanagiotis C, et al. Real-time dynamic strain sensing in optical fibers using artificial neural networks. Opt Express, 2019, 27: 7405
20 Wang Y F, Liu Q W, Li B Z, et al. Boosting the data processing speed by artificial neural network in distributed fiber-optic sensor. In: Proceedings of Optical Fiber Sensors Conference 2020 Special Edition, Washington, 2021
21 Li H, Fan C Z, Liu T, et al. Time-slot multiplexing based bandwidth enhancement for fiber distributed acoustic sensing. Sci China Inf Sci, 2021, 65: 119303
22 Liang Y X, Lin S T, Wang Z N, et al. Impulse response restoration of fiber Rayleigh scattering channel with double complementary pulses and deep learning. In: Proceedings of Asia Communications and Photonics Conference (ACP) and International Conference on Information Photonics and Optical Communications (IPOC), Beijing, 2020. 1–3
23 Liang Y X, Wang Z N, Lin S T, et al. Experimental demonstration of phase-sensitive OTDR with adaptive probe-pulse modulation. In: Proceedings of Optical Fiber Communication Conference (OFC), Washington, 2021
24 Karanov B, Chagnon M, Thouin F, et al. End-to-end deep learning of optical fiber communications. J Lightwave Technol, 2018, 36: 4843–4855
25 Wang F, Bian Y M, Wang H C, et al. Phase imaging with an untrained neural network. Light Sci Appl, 2020, 9: 77
26 Ravuri S, Lenc K, Willson M, et al. Skilful precipitation nowcasting using deep generative models of radar. Nature, 2021, 597: 672–677
27 Cho K, van Merrienboer B, Gulcehre C, et al. Learning phrase representations using RNN encoder-decoder for statistical machine translation. In: Proceedings of the Conference on Empirical Methods in Natural Language Processing (EMNLP), Doha, 2014. 1724–1734
28 Qian H, Luo B, He H J, et al. Phase demodulation based on DCM algorithm in Φ-OTDR with self-interference balance detection. IEEE Photon Technol Lett, 2020, 32: 473–476
29 Chen D, Liu Q W, He Z Y. Phase-detection distributed fiber-optic vibration sensor without fading-noise based on time-gated digital OFDR. Opt Express, 2017, 25: 8315
30 Wu Y, Wang Z N, Xiong J, et al. Interference fading elimination with single rectangular pulse in Φ-OTDR. J Lightwave Technol, 2019, 37: 3381–3387
31 Guerrier S, Dorize C, Awwad E, et al. Introducing coherent MIMO sensing, a fading-resilient, polarization-independent approach to Φ-OTDR. Opt Express, 2020, 28: 21081
32 Pastor-Graells J, Martins H F, Garcia-Ruiz A, et al. Single-shot distributed temperature and strain tracking using direct detection phase-sensitive OTDR with chirped pulses. Opt Express, 2016, 24: 13121
33 Chen D, Liu Q W, Wang Y F, et al. Fiber-optic distributed acoustic sensor based on a chirped pulse and a non-matched filter. Opt Express, 2019, 27: 29415
34 Xiong J, Wang Z N, Wu Y, et al. Single-shot COTDR using sub-chirped-pulse extraction algorithm for distributed strain sensing. J Lightwave Technol, 2020, 38: 2028–2036